Human Retinal Pigment Epithelium: In Vivo Cell Morphometry, Multispectral Autofluorescence, and Relationship to Cone Mosaic

Charles E. Granger,[1,2] Qiang Yang,[1] Hongxin Song,[3] Kenichi Saito,[4] Koji Nozato,[4] Lisa R. Latchney,[5] Bianca T. Leonard,[6] Mina M. Chung,[1,5] David R. Williams,[1,2] and Ethan A. Rossi[6,7]

[1]Center for Visual Science, University of Rochester, Rochester, New York, United States
[2]The Institute of Optics, University of Rochester, Rochester, New York, United States
[3]Beijing Institute of Ophthalmology, Beijing Tongren Eye Center, Beijing Tongren Hospital, Capital Medical University, Beijing Key Laboratory of Ophthalmology and Visual Sciences, National Engineering Research Center for Ophthalmic Equipment, Beijing, China
[4]Canon U.S.A., Inc., Melville, New York, United States
[5]Flaum Eye Institute, University of Rochester Medical Center, Rochester, New York, United States
[6]Department of Ophthalmology, School of Medicine, University of Pittsburgh, Pittsburgh, Pennsylvania, United States
[7]Department of Bioengineering, Swanson School of Engineering, University of Pittsburgh, Pittsburgh, Pennsylvania, United States

Correspondence: Ethan A. Rossi, Department of Ophthalmology, University of Pittsburgh School of Medicine, 203 Lothrop Street, Pittsburgh, PA 15213, USA; rossiea@pitt.edu.

Submitted: April 27, 2018
Accepted: October 18, 2018

Citation: Granger CE, Yang Q, Song H, et al. Human retinal pigment epithelium: in vivo cell morphometry, multispectral autofluorescence, and relationship to cone mosaic. *Invest Ophthalmol Vis Sci*. 2018;59:5705–5716. https://doi.org/10.1167/iovs.18-24677

Purpose. To characterize in vivo morphometry and multispectral autofluorescence of the retinal pigment epithelial (RPE) cell mosaic and its relationship to cone cell topography across the macula.

Methods. RPE cell morphometrics were computed in regularly spaced regions of interest (ROIs) from contiguous short-wavelength autofluorescence (SWAF) and photoreceptor reflectance images collected across the macula in one eye of 10 normal participants (23–65 years) by using adaptive optics scanning light ophthalmoscopy (AOSLO). Infrared autofluorescence (IRAF) images of the RPE were collected with AOSLO in seven normal participants (22–65 years), with participant overlap, and compared to SWAF quantitatively and qualitatively.

Results. RPE cell statistics could be analyzed in 84% of SWAF ROIs. RPE cell density consistently decreased with eccentricity from the fovea (participant mean ± SD: 6026 ± 1590 cells/mm^2 at fovea; 4552 ± 1370 cells/mm^2 and 3757 ± 1290 cells/mm^2 at 3.5 mm temporally and nasally, respectively). Mean cone-to-RPE cell ratio decreased rapidly from 16.6 at the foveal center to <5 by 1 mm. IRAF revealed cells in six of seven participants, in agreement with SWAF RPE cell size and location. Differences in cell fluorescent structure, contrast, and visibility beneath vasculature were observed between modalities.

Conclusions. Improvements in AOSLO autofluorescence imaging permit efficient visualization of RPE cells with safe light exposures, allowing individual characterization of RPE cell morphometry that is variable between participants. The normative dataset and analysis of RPE cell IRAF and SWAF herein are essential for understanding microscopic characteristics of cell fluorescence and may assist in interpreting disease progression in RPE cells.

Keywords: adaptive optics, retinal pigment epithelium, autofluorescence, retinal imaging, photoreceptors

The cells of the retinal pigment epithelium (RPE) have many functions vital to maintaining the health and function of the retina and overlying photoreceptors,[1] and are involved in several retinal diseases, including age-related macular degeneration (AMD).[2] Clinical imaging technologies such as confocal scanning laser ophthalmoscopy (cSLO),[3] optical coherence tomography (OCT),[4] and fundus autofluorescence[5–7] are useful for detecting and monitoring gross RPE disruptions such as drusen[8] or geographic atrophy.[9,10] However, in vivo imaging of the RPE with cellular-level resolution, achieved through the use of adaptive optics[11] (AO), offers the potential to detect finer spatial changes and monitor them over shorter timescales.

Morgan et al. have demonstrated that short-wavelength autofluorescence (SWAF) imaging methods from cSLO[5,6] could be adapted to image individual RPE cells[12,13] in adaptive optics scanning light ophthalmoscopy (AOSLO). However, obtaining high-quality images in normal humans was difficult owing to many factors, including chromatic aberration and light safety concerns. Though additional AO techniques have since been used to image RPE cells, a simple, robust, and repeatable solution has been elusive. Reflectance imaging is impeded by the strong signal from overlying photoreceptors, as demonstrated by Roorda et al.,[14] who imaged RPE cells in cone-rod dystrophy patients in locations where photoreceptors were absent. Dark field imaging[15] in AOSLO has circumvented this

masking effect, but its repeatability and utility in areas outside the fovea appears limited.[16] RPE imaging with AO-OCT has been demonstrated in a limited number of subjects and locations,[17,18] but may be computationally challenging and time prohibitive, as recent results have required 3D registration of volumes acquired over multiple time intervals. Finally, RPE cells have been imaged in AOSLO by using the fluorescence of intravenously injected indocyanine-green (ICG) that is absorbed by the cells,[19] but this method is invasive and ICG may be toxic to RPE cells.[20,21]

We previously have demonstrated AO SWAF imaging in AMD patients,[22] but to date SWAF imaging of individual RPE cells has only been shown in a limited number of human participants and locations,[13,15,22] leaving the normative RPE morphometry drastically undercharacterized in this modality. Here we capitalize on recent technical developments in AOSLO system design[23] and eye-tracking[24] to further improve AO SWAF imaging (Yang Q, et al. *IOVS* 2015;56:ARVO E-Abstract 5971), increasing safety and substantially improving efficiency. With these improvements, we image across the macula in normal eyes for eccentricity-dependent quantitative analysis of RPE and photoreceptor cells within and between participants, including RPE cell size and density and the ratio of cone photoreceptors to RPE cells. Photoreceptor-to-RPE cell ratios may be a relevant biomarker to facilitate diagnosis or improve our understanding of disease risk, but have only been investigated in a handful of ex vivo[25–27] and in vivo[15,16,18] investigations with limited locations or participant number and age range. This study expands upon previous studies with data from 10 normal participants whose ages span 5 decades, thoroughly characterized within an average of 25 regions of interest (ROIs) across the horizontal meridian.

Finally, we demonstrated that infrared autofluorescence (IRAF) can be used to image individual RPE cells in AOSLO (Granger CE, et al. *IOVS* 2017;58:ARVO E-Abstract 3429), presumably from exciting fluorescence from melanin and/or melanosomes[7,28,29]; this was corroborated by a recent report from another laboratory that developed the approach independently.[16] IRAF and SWAF image separate molecules potentially relevant to human disease: bisretinoids (e.g., A2E[30,31]) and their aggregates (e.g., lipofuscin[32,33]) in SWAF, and melanin in IRAF.[34,35] Microscopic differences between modalities may reveal disease characteristics and inform comparisons of IRAF and SWAF fundus images common in the clinic.[36–38] We examined this in normal eyes, using AO IRAF and SWAF to provide cellular and subcellular comparisons of the spatial distribution of fluorophores. The results of this study allowed us to (1) compare each modality as a clinical evaluation tool and (2) define the in vivo morphometry and autofluorescence (AF) characteristics of the normal human RPE cell mosaic. The former is necessary from a practical standpoint as we look toward the future tools needed to evaluate modern treatments, such as gene therapy and stem cell approaches to vision restoration. The latter is critical as a means of comparison for our ongoing and future work that aims to understand the changes to the RPE at the level of single cells in AMD, Stargardt's macular dystrophy, and other retinal diseases that involve RPE dysfunction and cause severe vision loss.

Methods

Participants

A total of 13 participants (age range, 22–65 years; mean ± standard deviation, 37 ± 15 years) were recruited from the University of Rochester community. Verbal and written informed consent was obtained following an explanation of experimental procedures and risks. Research procedures were conducted according to the tenets of the Declaration of Helsinki and approved by the University of Rochester Research Participants Review Board. Upon comprehensive eye examinations performed by an ophthalmologist (one of the authors [MMC]), all participants aside from NOR076 had normal, healthy-appearing retinas and clear anterior optics. A small area between the fovea and optic nerve head was identified in NOR076 as potential drusen in infrared reflectance cSLO and OCT. To scale images across modalities, axial lengths were measured with an IOLMaster (Zeiss Meditec, Dublin, CA, USA) or Lenstar LS 900 (Haag-Streit AG, Bern, Switzerland). Cycloplegia and pupil dilation were induced with one drop each of 2.5% phenylephrine hydrochloride and 1% tropicamide. Clinical images were acquired on all participants, including color fundus photographs, infrared reflectance, and blue autofluorescence (λ_{exc} = 488 nm) in cSLO (Heidelberg Spectralis HRA+OCT; Heidelberg Engineering, Heidelberg, Germany). IRAF fundus images (λ_{exc} = 785 nm) were acquired on the same instrument for participant NOR076 and those imaged with AO SWAF and AO IRAF in the same day.

AOSLO Instruments

The AOSLOs used for these experiments are described in detail elsewhere.[23,39] SWAF imaging was performed with an AOSLO designed for clinical use,[23] with integrated wide-field subsystem, beam steering, and active eye-tracking and image stabilization.[24] Field of view was 1.75° × 1.75° with an ~20-Hz frame rate; sinusoidal distortion was rectified digitally.[40] Near-infrared (NIR) reflectance (796 nm) and SWAF (532 nm excitation) images were acquired with equipment described previously.[22] A −1 diopter (D) vergence difference between the reflectance and SWAF sources was set to counter longitudinal chromatic aberration in the human eye,[41] with the intention of exciting RPE lipofuscin AF while the NIR channel remained focused on the photoreceptors to provide a strong spatial signal for active image stabilization, coregistration, and averaging. To minimize effects of longitudinal chromatic aberration variability amongst participants, the excitation beam was reduced to 3 mm at the entrance pupil for increased depth of focus.

A second AOSLO[22] was modified for IRAF by adding a detection channel to collect wavelengths between 800 and 900 nm. This band was chosen from clinical instrument parameters[7] and the spectra of melanin IRAF.[42] Wavefront sensing was shifted to 940 nm with a 940/10-nm bandpass filter placed at the fiber output to reduce leakage of spontaneous emission into the IRAF detection channel. A 796-nm NIR superluminescent diode was used for IRAF excitation and NIR reflectance imaging over a 1.5° × 1.5° field of view with a 769/41-nm bandpass filter at the fiber output. The reflectance channel collected wavelengths <795 nm through an ~1.2 Airy disk diameter pinhole for navigation and coregistration of the low-signal IRAF channel. Two bandpass filters were used in the IRAF detection channel; a narrow-bandwidth 832/37-nm filter designed for ICG fluorescence, and a custom-designed broader-bandwidth 853/96-nm filter. Confocal pinholes for the IRAF channel were 2 to 3 Airy disk diameters.

SWAF Imaging

Safe and efficient SWAF imaging requires maximizing the excitation and detection of the weak SWAF signal while minimizing visible light exposures. To accomplish this, we used a systematic imaging routine with automated optimization of the deformable mirror (DM) focus and computer-controlled

Investigative Ophthalmology & Visual Science

placement of the SWAF channel confocal pinhole.[22] Exposures were 30 seconds, often with real-time optical stabilization and digital image registration[23,24] engaged, which displayed the AF image integration and informed if repeated exposures or parameter adjustments were necessary. Optimization routines were repeated when image quality decreased. A ∼25° horizontal strip of retina was imaged in one eye of each participant, crossing the fovea and center of fixation, with roughly 0.5° of overlap between adjacent images. Images were typically acquired in two sessions totaling 2 to 4 hours, with additional sessions for three participants. In one participant, a larger area covering ∼11° × 15° was imaged over eight sessions totaling 10.5 hours. Additional methodologic details are provided in Supplementary information.

IRAF Imaging

For IRAF, the NIR source was focused to obtain a high-contrast image of the photoreceptors; the relatively elongated axial point spread function at the retina was assumed to allow for simultaneous IRAF excitation. The IRAF detector with attached pinhole was automatically positioned as in the SWAF system, and 50- to 75-second image sequences were captured. Image sequences were desinusoided, coregistered, and averaged as described previously,[12] combining data from both forward and backward scans. Contiguous IRAF was acquired in seven eyes, with ∼50% overlap between adjacent fields, usually over an area that tiled the fovea and included a temporal or nasal strip spanning between 10° and 15°. In one participant, a nasal area was imaged that included the small drusen identified in clinical images. To compare modalities, IRAF and SWAF images were also acquired at the same retinal location in three participants. At each location, a 60-second IRAF image sequence was acquired before and after a 30-second SWAF sequence, all using similar field size. Image sequences at each location were acquired within a short time interval (≤100 minutes) and registered with the same reference frame to provide the best structural comparison between modalities.

Processing to Mitigate Transverse Chromatic Aberration Blur From Pupil Motion in SWAF Images

During SWAF imaging, pupil shifts from head and eye motion generate dynamically varying transverse chromatic aberration (TCA)[43] between the two imaging channels. While previous studies have assumed TCA has a negligible effect on image quality,[13,22] our real-time averaging revealed that time-varying TCA from pupil motion causes blur in the AF channel during exposures because the coregistration method assumes a fixed position difference between the NIR and AF channels. We used a simple postprocessing method (Yang Q, et al. *IOVS* 2015;56:ARVO E-Abstract 5971) to mitigate this effect and improve image quality. Image sequences were split into 8 to 10 short segments, where each was coregistered and averaged by using the same NIR reference frame. The images from each segment were then registered by cross-correlation and averaged to produce a higher signal-to-noise ratio image with reduced TCA blur. Segments with poor image quality from excessive head or eye motion and/or tear film degradation were omitted from final averages.

Photoreceptor and RPE Cell Analyses

SWAF images were overlaid on fundus photos and stitched by using Adobe Photoshop CS6 (Adobe Systems, Inc., San Jose, CA, USA) to create contiguous montages for quantitative analysis (Supplementary Figs. S1–S10). Simultaneously acquired AO photoreceptor images were aligned to the RPE montage by using vascular landmarks. Image processing was limited to brightness and contrast adjustments and removal of edge artifacts between adjacent fields. To reduce the dataset into manageable quantifiable areas, we placed 150 μm × 150 μm ROIs at ∼250-μm intervals centered on the fovea (defined as the center of the foveal avascular zone), as shown in Supplementary Figure S11. ROIs were relocated, if necessary, to avoid blood vessels and/or areas of poor image quality.

Semiautomated custom segmentation software[44] and photoreceptor marking software (based on a previously published algorithm[45]) produced binary images of RPE cell boundaries and photoreceptor coordinates for each ROI. Automated RPE segmentation errors were manually corrected as previously described,[22] where segmentation within ROIs was limited to cell boundaries that could be discerned confidently by a grader. Edge cells with a portion of the area outside the ROI were excluded. Custom MATLAB (The MathWorks, Inc., Natick, MA, USA) programs analyzed binary images cell-by-cell, computed ROI statistics, and plotted them as a function of eccentricity for each participant. ROI mean cell area and standard deviation were computed from individual cell areas and adjusted to include the area of segmented cell borders. Mean cell density was computed as the inverse of mean cell area. ROI cell count and fill factor provided metrics of image quality and segmentation ability, where fill factor was computed as the ratio of total segmented cell and border area to ROI area. Fill factor was always <1 owing to the removal of aforementioned edge cells, in addition to regions where cell borders were indeterminate; however, the metric still allowed for relative comparison within and between participants. The number of cones within each RPE cell was used to calculate the mean cone-to-RPE ratio. Further details are provided in Supplementary information.

Light Safety

A computer-controlled shutter regulated visible light exposures; acquisition software calculated the cumulative exposure duration at each location and closed the shutter before our exposure limit was reached. The combination of stabilization, tightly coupled light delivery and data acquisition, and AF channel optimization allowed for SWAF RPE imaging with excitation beam powers of only 10 to 15 μW at the cornea. For IRAF imaging, the 796-nm power at the cornea was comparable to typical photoreceptor reflectance imaging levels (∼150 μW). Standard exposures in both IRAF and SWAF were ≤4% of the American National Standards Institute (ANSI) maximum permissible exposure[46] for all combined sources, allowing ample room for repeated exposures and overlapping contiguous imaging. Furthermore, typical SWAF retinal exposures were only ∼10% of those necessary to produce AF reduction in macaques.[47] To minimize cumulative light exposures, clinical imaging was performed on separate days from AO SWAF imaging. Light sources and safety calculations are described in detail in Supplementary information.

Results

SWAF Imaging and RPE Cell Analysis

After focus and pinhole optimizations, a single 30-second exposure was typically adequate for a high signal-to-noise ratio SWAF image. At least five additional exposures could typically be acquired before reoptimization was necessary, which we performed when image quality appeared to decrease or whenever the participant exited and re-entered the chin and

Investigative Ophthalmology & Visual Science

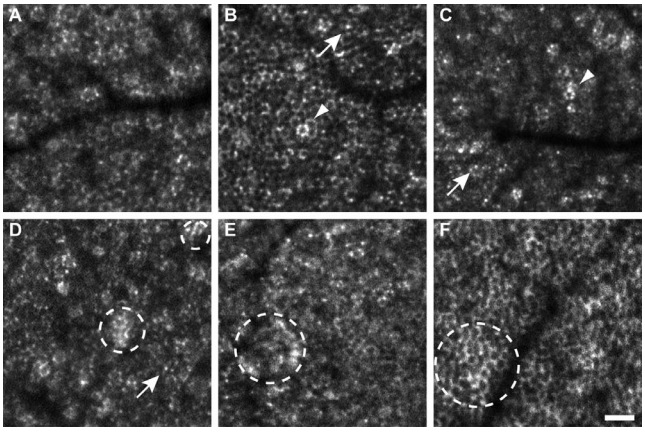

Figure 1. Variations in RPE cell morphology visualized with SWAF. Cell boundaries consisted of distinct punctate spots of AF (e.g., **A**, **D**), presumably individual lipofuscin granules (*arrows*), or more complete rings of AF (e.g., **B**, **F**). Individual hyper-AF cells (*arrowheads*) and hyper-AF patches (*dashed circles*) were observed. (**A**–**F**) From participants NOR064, NOR053, NOR057, NOR063, NOR047, and NOR073, respectively. *Scale bar*: 50 μm.

forehead rest. TCA correction considerably improved image quality, even in image sequences with moderate fixational eye motion. The subjective RPE image quality was usually best at a plane of focus different from the plane of peak AF mean pixel value (MPV). We recorded the difference between these focal planes from 340 images between all participants and averaged them over 500 μm eccentricity bins (Supplementary Fig. S12). The typical defocus offset across the macula was 0.1 D sclerad of peak AF, tending to increase in the nasal region, whereas the fovea was more variable and ranged from −0.05 to 0.05 D.

Microscopic SWAF and cellular structure was visible across the imaged area in all 10 participants (Supplementary Figs. S1–S10), with diverse morphologies observed. Cell boundaries were defined by either a ring of contiguous or punctate AF (Fig. 1), presumably from individual lipofuscin granules, where AF gaps or irregularities often caused errors in automated segmentation. Individual hyper-AF cells and patches of hyper-AF that did not appear confined to individual cells (Fig. 1) were also observed. These patches were often also visible in cSLO fundus images (Supplementary Fig. S13). RPE cell visibility varied across the retina within and between participants, particularly in the fovea and parafovea, as illustrated qualitatively in Figure 2 and in plots of ROI-segmented cell count and fill factor in Figure 3. Between participants, cells could be segmented in 140 of 145 ROIs at eccentricities >2 mm, with a mean fill factor of 0.5, while both the percentage of segmentable ROIs (106 of 148) and mean fill factor (0.38) decreased between ±2 mm. Fill factor variability was greatest at the fovea and lowest at temporal locations. Some locations did not yield cellular structure even with repeated focus and detector optimization, indicating that other factors also affect cell visibility.

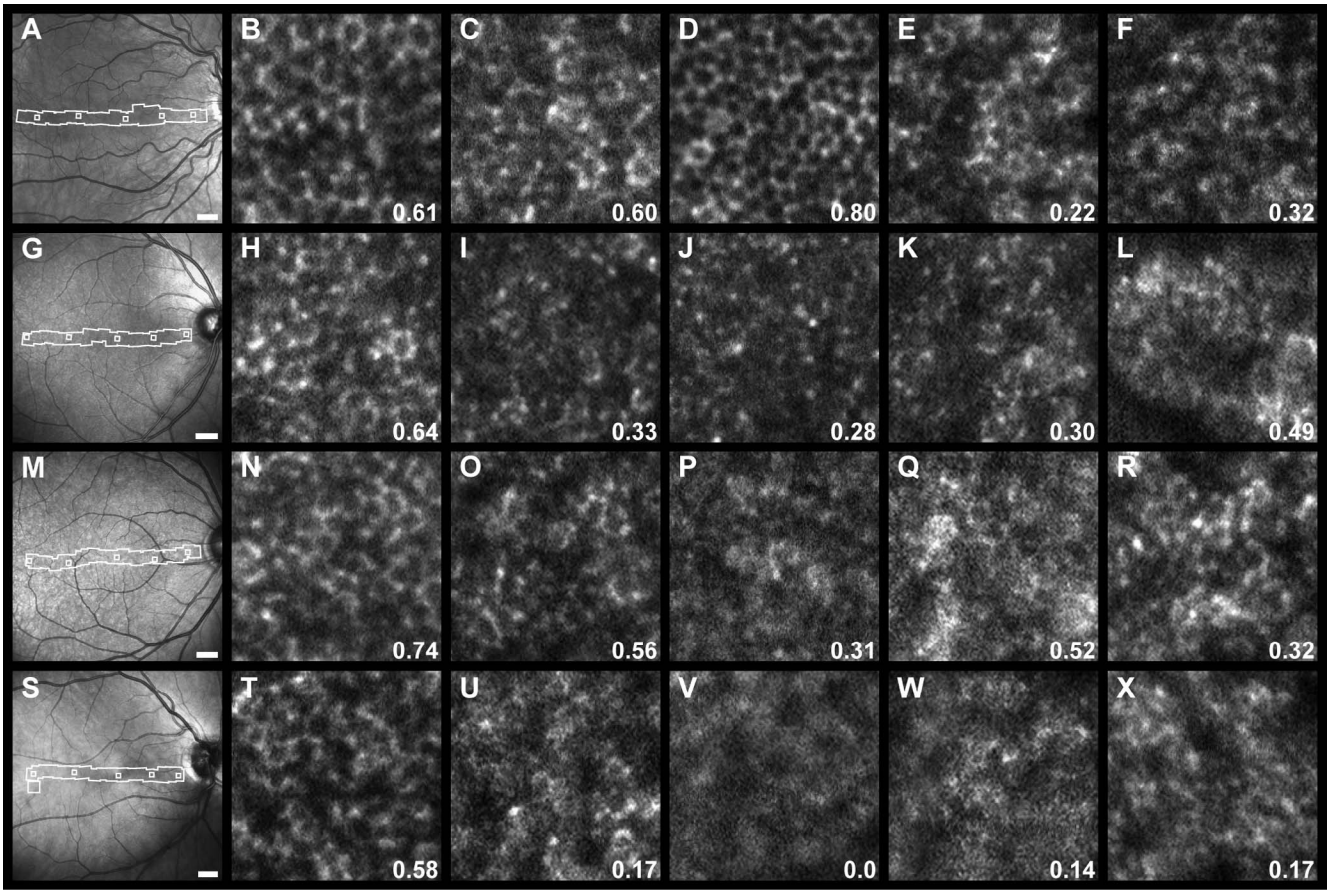

Figure 2. Comparison of AO SWAF in four participants (*top* to *bottom* row, with increasing age: NOR053, NOR063, NOR047, and NOR011), illustrating range of image quality within and between participants. SWAF ROIs at similar eccentricities are displayed in columns along with fill factor values. ROI locations are indicated by boxes within the montaged area (*white outlines*) in fundus images. RPE cells were consistently visible at larger eccentricities, even when foveal image quality was poor. *Scale bars*: 1 mm for fundus images. All ROIs are 150 × 150 μm.

Investigative Ophthalmology & Visual Science

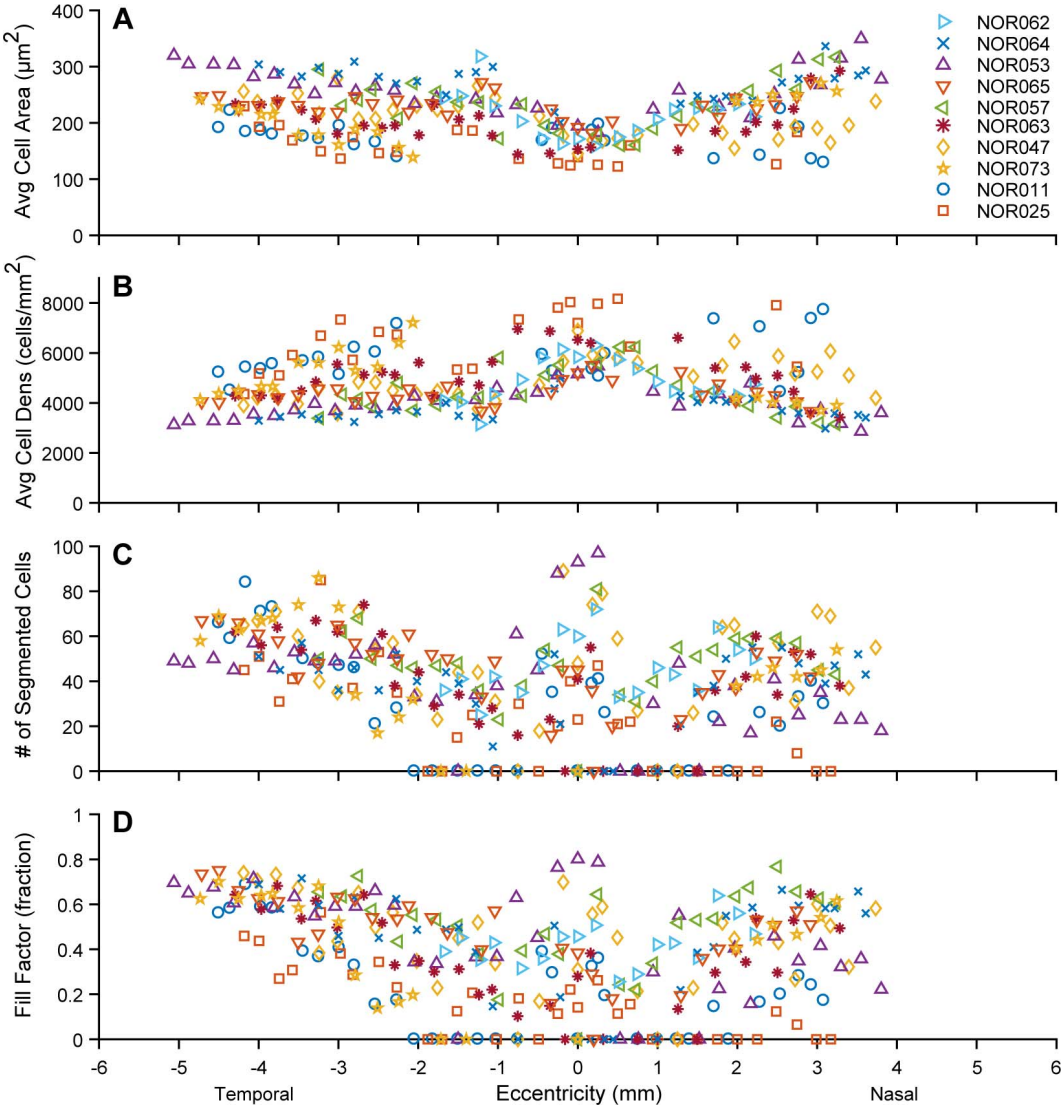

Figure 3. Measured SWAF RPE cell statistics for participants, listed in order of increasing age in the legend. Cell area increases with eccentricity (**A**), where the rate of increase differed between participants. Measured cell densities (**B**) in the three oldest participants were among the highest, though these cells were typically difficult to segment. (**C**, **D**) Cell segmentation was consistently greater in the periphery, particularly temporal locations, while the fovea exhibited high variability. Eighty-nine percent of ROIs with no segmented cells fell within ± 2 mm of the fovea and in the nasal retina, perhaps because of increased absorption and scatter due to melanin, vasculature, and/or maculopapillary nerve fiber bundles (in the nasal retina).

Despite variable cell visibility, a total of 11,309 RPE cells were segmented and analyzed across participants. Cell area increased with eccentricity in all participants (Fig. 3) and on average (Supplementary Fig. S14), though this was less pronounced in the nasal data of NOR011 and NOR025. The rate of increase differed markedly between individuals. In six participants, average RPE cell area increased ≥50% by 4 mm of eccentricity, whereas in NOR057 and NOR011 the increase was only ~25%. As average cell area increased with eccentricity, average cell density decreased: from 6026 ± 1590 cells/mm^2 at the fovea to 3757 ± 1290 cells/mm^2 and 4552 ± 1370 cells/mm^2 at 3.5 mm nasally and temporally, respectively. Interestingly, the three oldest participants typically had the greatest cell densities, with the highest (8172 cells/mm^2) observed in the fovea of the oldest participant. Participant phenotypic characteristics and select RPE cell densities (maximum and 3.5 mm temporally) are provided in the Table.

Cone-to-RPE Ratio Analysis

Mean cone-to-RPE cell ratio (Fig. 4) peaked at the foveal center (16.6 cones per RPE cell) with considerable variability between participants (between 10.3 and 24 cones per RPE cell), and decreased rapidly over 2 mm eccentricity to level off at ~1.5 cones per RPE cell with remarkable consistency between participants. Binned and averaged cone-to-RPE data were in good agreement with a theoretical cone-to-RPE ratio curve, generated by dividing previously reported cone density data[48] by the binned and averaged participant RPE density data in this study (assuming a linear fit to nasal and temporal density data, constrained to have the same density at foveal center). The exception was the foveal data point, where the measured ratio was much lower than the predicted ratio of 35, perhaps owing to an inability to fully resolve foveal cones in some participants and a large sampling window in a region of rapidly changing cone density.

Investigative Ophthalmology & Visual Science

Table. SWAF Study Participant Phenotype Characteristics and Select Data

Particip.	Age, y	Sex	Axial Length, mm	N_{tot}	Maximum Foveal Ecc., mm	Maximum Foveal RPE Density, Mean ± SD, Cells/mm²	Maximum Foveal *n*	Temporal Ecc., mm	Temporal RPE Density, Mean ± SD, Cells/mm²	Temporal *n*
NOR062	23	F	23.85	782	0	6308 ± 1140	72	–	–	–
NOR064	25	F	24.12	1088	0.2	4994 ± 860	21	3.5	3517 ± 1440	52
NOR053	27	F	24.07	1446	0.25	5476 ± 1230	97	3.6	3720 ± 1060	53
NOR065	27	F	24.28	1375	0.2	5503 ± 1030	36	3.5	4328 ± 1180	42
NOR057	35	F	23.76	1284	0.25	5589 ± 1230	81	3.2	3390 ± 1040	50
NOR063	35	M	23.25	1164	0	6527 ± 1880	41	3.5	4480 ± 1360	54
NOR047	41	M	23.61	1565	0	6892 ± 2380	48	3.5	3962 ± 1140	60
NOR073*	55	F	22.51	932	–	–	–	3.5	5622 ± 1730	74
NOR011	62	F	25.52	959	0.25	5731 ± 1130	39	3.4	5682 ± 1340	50
NOR025	65	M	24.79	714	0.1	8035 ± 2100	40	3.6	5918 ± 1930	41
			Participant mean†		0	6026 ± 1590	1039	3.5	4552 ± 1370	671

Ecc., eccentricity; n = number of cells in ROI; N_{tot}, total cells analyzed in dataset; Particip., participant.
* Only temporal and nasal peripheral retina imaged, OS eye (all other eyes OD).
† Binned and averaged participant data (500-µm bins, contains additional ROIs).

IRAF Imaging

IRAF images revealed a cellular structure resembling the RPE mosaic (Fig. 5). Cell appearance was similar to that seen in SWAF, with hypo-AF center and hyper-AF surround. IRAF signal and cell sharpness were best at the focal plane where the photoreceptors in the reflectance image appeared brightest and sharpest. Of seven participants imaged, individual cells were clearly visible in the fovea of four participants, and nasal and temporal locations of six participants, up to the furthest eccentricity imaged of 15°. The participant with no visible cells was the first to be imaged with AO IRAF, and we suspect our experimental setup was not yet optimized. Contrast between cell center and surround varied between participants and even between cells within a single image, affecting cell visibility, as seen in Figure 5. Cells were particularly difficult to distinguish between 0.5 and 2 mm of eccentricity, following the trend seen in SWAF. IRAF signal was greatest in the fovea and decreased rapidly to plateau at approximately 50% of the foveal signal by 5°, consistent with the gross IRAF pattern seen in clinical cSLO.

AO IRAF revealed microstructure in the region of drusen that was not visible in clinical images. In fundus images, the drusen region appears primarily hyporeflective in NIR reflectance and faintly hypo-AF in IRAF (Figs. 6A, 6B),

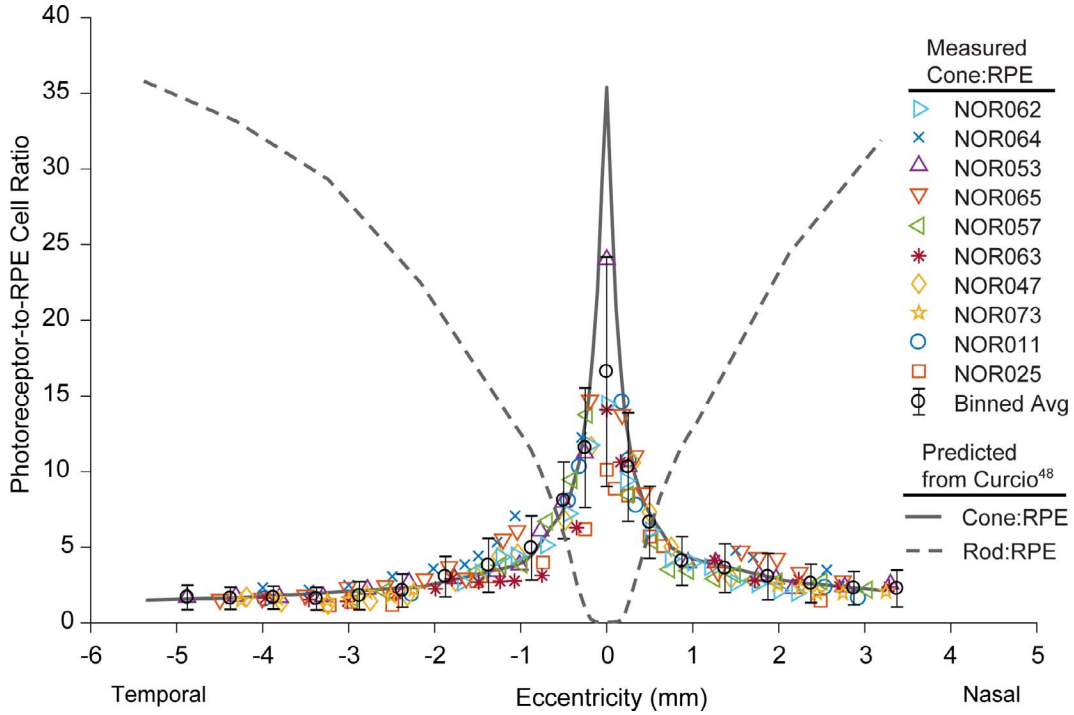

Figure 4. Plot of measured cone-to-RPE cell ratio across the macula, showing individual participant ROI data (*colored markers*) and binned and averaged data (*black circles*). The shape and interparticipant variability are dominated by cone density rather than RPE density. With the exception of foveal center, our data agree with the expected ratio (*solid gray line*), generated by using previously published cone density data[48] and the RPE density data in this study. The theoretical rod-to-RPE ratio curve (*dashed gray line*) is also shown for reference, generated by using published rod density data.[48]

Investigative Ophthalmology & Visual Science

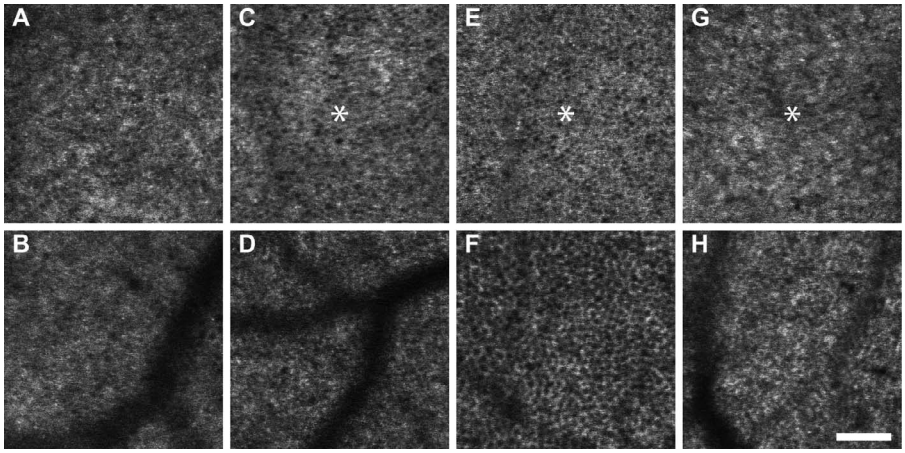

Figure 5. AO IRAF images of the RPE mosaic (NOR079 [**A**, **B**], NOR065 [**C**, **D**], NOR053 [**E**, **F**], and NOR063 [**G**, **H**]). Cellular structure with hyper-AF borders and hypo-AF centers form a mosaic in images, except for (**G**), where cells are not clearly visible. *Asterisks* mark the peak cone density location on foveal center images (**C**, **E**, **G**). (**A**) Centered 0.2 mm superiorly to foveal center. (**B**, **D**, **F**, **H**) At 1.3 mm nasally, 2.7 mm nasally, 3.2 mm temporally, and 3.1 mm temporally, respectively. *Scale bar*: 100 μm.

approximately 500 μm wide. In the same region, small bumps in the photoreceptor-RPE reflective bands of the OCT B-scan are seen. AO reflectance shows the imaged area dominated by relatively normal-appearing cones (Fig. 6D) with small areas of hyporeflectance and/or decreased cell contrast. AO IRAF shows a seemingly regular RPE mosaic disrupted near the center of the image by small (10-20–μm diameter) circular hyper-AF structures interspersed with areas devoid of AF. Individual RPE cells were visible up to the borders of these regions and even between disrupted regions.

Comparison of RPE Cells in IRAF and SWAF Imaging

Figure 7 shows an example of IRAF and SWAF images acquired in close succession at one of four locations eligible for comparison. Increased NIR transmission made blood vessels less apparent in IRAF, while hyper-AF patches and points were more frequent in SWAF. Though developed for SWAF images, our segmentation algorithm[44] performed similarly when applied to IRAF images, despite apparent decreased cell contrast as compared to SWAF. Segmentation analysis could only be performed at three locations, where results are listed in Supplementary Table S2. Mean cell densities agreed within ≤3.5% between modalities at each location. Cell locations were also in agreement (Fig. 7C). Between all three locations, 808 of 917 segmented SWAF cell centroids fell within IRAF segmented regions, 84% of which were colocalized with IRAF centroids to ≤4 μm (approximately half the mean cell radius). More cells were consistently segmented in IRAF (12%–32% more than SWAF), particularly in regions beneath blood vessels (Fig. 7C). The increased cell count in IRAF corresponded to an increased fill factor as compared to SWAF, explaining the consistent density measurement between modalities.

Differences in the macroscopic and microscopic pattern of IRAF and SWAF were observed. Punctate hyper-AF spots were not always colocalized between modalities (Figs. 8B, 8C). Figure 8B shows instances of hyper-AF punctate spots in IRAF with size and location consistent with cones in reflectance. This colocalization was inconsistent across the image and at other locations (Fig. 8F). Interestingly, the spots were not observed in the second IRAF image acquired 1.3 hours later. Regions of hyper-AF in SWAF spanning multiple cells were observed in all three participants, but similar patches of IRAF hyper-AF were not obvious. Regions of SWAF hyper-AF typically showed no noticeable differences in IRAF intensity at the same location (Figs. 8J–L, dashed ovals), though instances of IRAF hypo-AF coinciding with SWAF hyper-AF (Figs. 8N–P, highlighted regions) were observed.

IRAF Reduction

An 8% to 13% reduction in IRAF was measured in postexposure cSLO fundus images at four locations between two participants that underwent successive AO IRAF and SWAF imaging (Supplementary Fig. S15), with cumulative 790-nm retinal radiant exposures (RREs) ranging from 17.1 to 27.7 J/cm^2 (Supplementary Table S3). These RREs were only 10% to 15% of those observed to cause IRAF reduction in humans in a previous study,[49] well below ANSI limits. No reduction was detected at unexposed control locations. The reduction is visible by eye when comparing the pre- and postexposure images but may not be obvious when examining postexposure images in isolation. Detailed methods and discussion of results are provided in Supplementary information.

Discussion

SWAF Imaging

The improvements in the AOSLO for SWAF imaging demonstrated here increase both safety and efficiency in comparison with previous in vivo SWAF studies and demonstrate progression toward the use of AO SWAF in the clinic. However, further improvements are necessary, including reducing time for total imaging and manual segmentation correction. The clinical potential of AO SWAF is further discussed in Supplementary information. Maintaining a low visible light RRE allows time to optimize imaging parameters and permits contiguous overlapping imaging. The image quality improvement from TCA post processing strongly suggests that TCA can induce nonnegligible blur when coregistering in SWAF. This phenomenon is not unique to SWAF and will occur when the pupil moves away from the achromatic axis in any multiwavelength imaging system. RPE image quality improvement from the scleral DM defocus from peak AF is likely due to improved contrast when AF at the cell margin is in sharp relief to the central hypo-AF region of the cell (where the lipofuscin-free nucleus resides), where overall AF signal is slightly reduced.

Investigative Ophthalmology & Visual Science

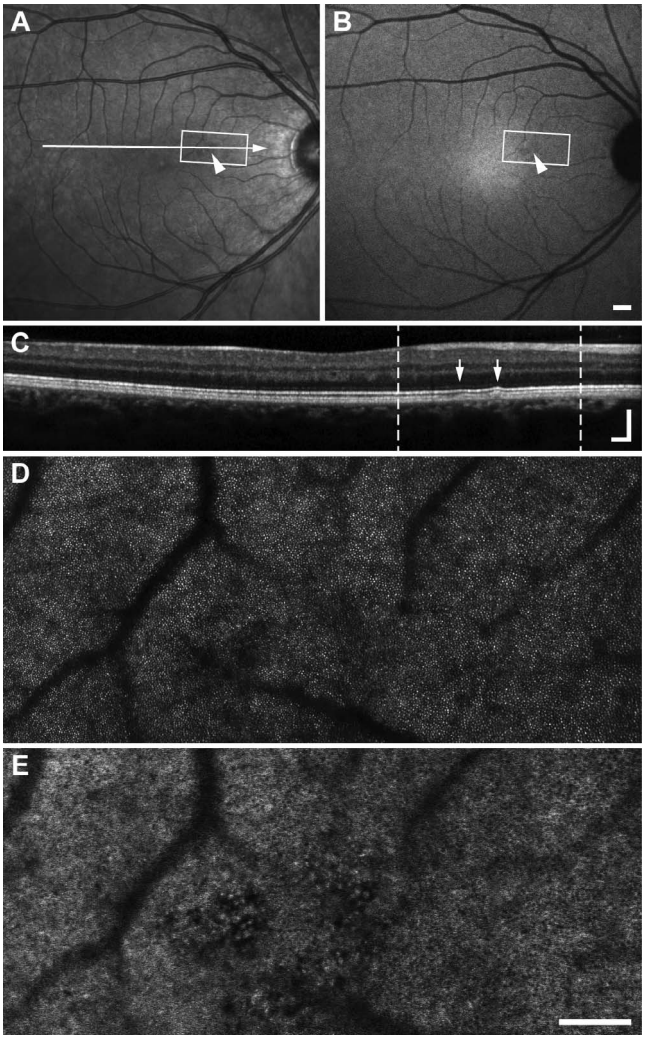

FIGURE 6. In participant NOR076, cSLO NIR reflectance (**A**) and IRAF (**B**) images show a small region of variable reflectivity and subtle hypo-AF (*arrowheads*). The OCT B-scan (**C**) corresponding to the *arrow* in (**A**) shows small bumps in the outer retina (*arrows*) suggestive of drusen. *White boxes* in (**A**, **B**), and *dashed lines* in (**C**) denote the region imaged with AO. Photoreceptors in AO NIR reflectance (**D**) appear relatively normal, with a cluster of hyporeflective cones near presumed drusen, consistent with the gross appearance in (**A**). Hyporeflective locations correspond to punctate hyper- and hypo-AF structures in AO IRAF montage (**E**) disrupting a normal-appearing RPE mosaic. *Scale bars*: 500 μm for (**A**, **B**) and 200 μm (**C**, vertical and horizontal, **D**, **E**).

While it is promising that RPE cells could be analyzed in 84% of ROIs across participants, understanding the source of reduced foveal and/or parafoveal cell visibility seen in six participants will be critical to greater success in future studies. Reduced foveal image quality may be due to difficulties in simultaneously obtaining optimal excitation of lipofuscin and reflectance imaging of the small cones at the foveal center with a fixed focus offset between the two sources. Lower SWAF signal in this region[5,6] from a higher concentration of melanin and lower concentration of lipofuscin within foveal RPE cells relative to peripheral cells[50,51] may increase noise and decrease contrast. The absorption of SWAF excitation and emission by blood certainly confounds cell visibility, though it is unclear why this may be amplified in the parafovea. Absorption from the macular pigment should be minimal for the 532-nm excitation light[52,53] and should not impact cell visibility in our setup.

SWAF RPE Cell Analysis

The trend of decreasing RPE cell density with increasing eccentricity from the foveal center agrees with previous studies,[19,26,27,54–58] and binned and averaged participant density data are generally in agreement with previous data (Supplementary Fig. S14), thus demonstrating the validity of RPE analysis across humans, using SWAF. The variability in RPE cell density between participants in this study and others may be expected when considering the normal variability in other visual system levels (e.g., cone density measurements[48,59]) and may contribute to conflicting conclusions regarding RPE cell loss with age.[25–27,54–58,60] This is supported by observations of relatively high densities in older eyes in other studies[26,57] in addition to our own. It may be argued that RPE characteristics are not easily generalized between participants, warranting further in vivo investigations for characterization and longitudinal study of RPE biometrics with age and in retinal diseases to better understand the differences between normal aging and early AMD.

Our ability to accurately quantify RPE cell metrics is limited by cell visibility and segmentability, where inaccuracies in segmentation due to irregular lipofuscin distribution could affect measurements. The manual correction of segmentation errors and removal of cells with uncertain borders helps mitigate such effects, as we note that cell density measurements were typically consistent between neighboring ROIs within participants and between participants at different eccentricities, even in foveal and parafoveal ROIs with low cell counts. This highlights the advantages of individual cell segmentation and shows potential for analysis in aged or diseased eyes where lipofuscin accumulation[57] and/or redistribution[61] can occur and degrade cell visibility. Full-resolution participant montages (Figs. S1–S10) are available online at the Dryad Digital Repository for those who wish to perform further analysis or test analysis software; our segmentation images and ROI locations are also available upon request. The improved fill factor at larger eccentricities for all participants, particularly in the temporal retina, suggests that cell visibility is affected more by regional retinal characteristics than the age or ocular quality of participants. These factors, along with other practical considerations (i.e., imaging and data analysis efficiency) are important in the evaluation of high-resolution SWAF RPE imaging as a clinical tool, which is discussed in Supplementary information.

Photoreceptor Analysis

A total of 78,029 photoreceptors were identified in our analysis, including 32,626 cones and 45,403 rods. Cone density analysis in this study was in good agreement with other studies, with exception of a lower mean foveal center density. This indicates that the smallest cones were not always completely resolved, which is not surprising as these cells are near the limits of the resolution of AOSLO.[62] Despite the identification of numerous rods in our images, directly computed rod densities indicated we were unable to identify and differentiate every rod within each ROI, therefore we did not report rod-to-RPE cell ratios here. The resemblance of the mean cone-to-RPE cell ratio plot (Fig. 4) to a cone density plot[48] highlights the relative flatness of RPE cell density across the macula compared to cones. Averaged across participants, our cone-to-RPE ratio data are generally in agreement with previous ex vivo studies and in vivo results recently reported by Liu et al.[16] Our lower-than-predicted foveal center ratio is shared with the latter study, and that of Dorey et al.,[25] who measured a ratio of 12.6 but acknowledge results may be

Investigative Ophthalmology & Visual Science

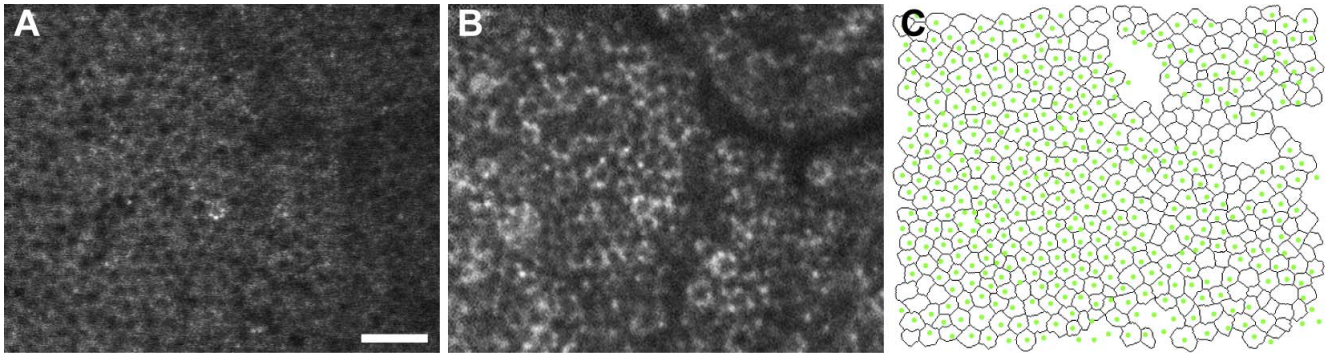

Figure 7. Comparison of the RPE mosaic imaged at the same location with IRAF (**A**) and SWAF (**B**). The overlay of SWAF-segmented cell centroids (*green dots*) on the IRAF-segmented image (*black outlines*) (**C**) shows colocalization of cells. Improved NIR transmission permits additional cells to be segmented beneath the blood vessel in IRAF, reflected in fill factors (0.83 and 0.73 for [**A**] and [**B**], respectively). Images acquired at 0.3 mm nasal eccentricity in participant NOR053a. *Scale bar*: 50 μm.

underestimated by estimating ratios from transverse sections. A smaller sampling window accurately positioned at the peak cone density and larger sample size (22 eyes) may explain a higher mean foveal center ratio of 24.09 measured by Gao and Hollyfield.[26] We point out that our limited foveal center ratios (ratio = 16.6 ± 7.6, $n = 4$) fall within their reported range of 11 to 44 cones per RPE cell.

A cone-to-RPE ratio of approximately 1 toward the edge of the macula and beyond is consistent in this study and others,[26,27] though it remains unclear why RPE cells seem to

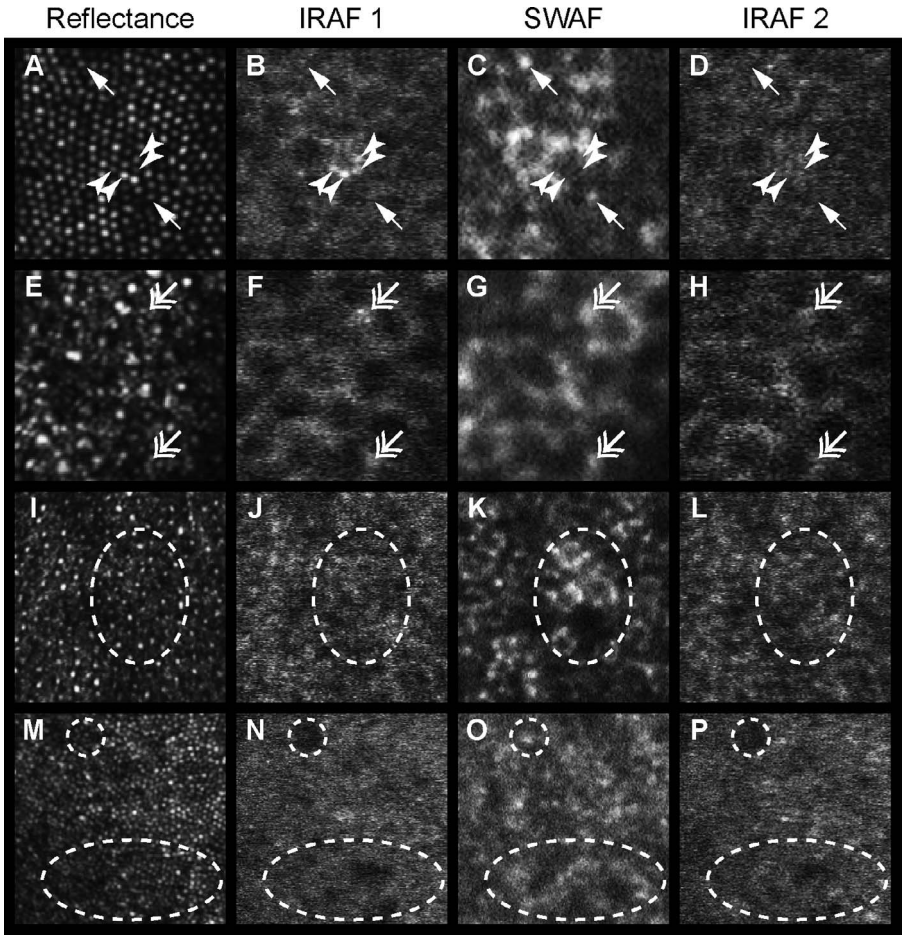

Figure 8. Microscopic SWAF and IRAF structure at the fovea (**A–D**) and 10° temporally (**E–H**) for participant NOR053, 10° temporally (**I–L**) in NOR063, and near foveal center (**M–P**) of NOR025. From *left* to *right*, columns show the NIR reflectance image, the first acquired IRAF image (IRAF 1), the SWAF image, and the second acquired IRAF image (IRAF 2). Incidences of colocalized (*double head arrows*) and noncolocalized (*arrows, arrowheads*) punctate hyper-AF between modalities were observed. Four distinct points of hyper-IRAF (*arrowheads*) in (**B**) have the same size and location of cones in reflectance (**A**), and are absent in the IRAF 2 image (**D**) acquired 1.3 hours later. The *dashed oval* in (**K**) shows a SWAF patch of hyper-AF and hypo-AF, while the IRAF images show no corresponding features at the same location. In contrast, (**O**) shows two patches (*dashed circle* and *oval*) of hyper-SWAF that appear to be hypo-AF in IRAF. (**A–H**) 75 × 75 μm. (**I–P**) 150 × 150 μm.

Investigative Ophthalmology & Visual Science

tend at least one cone, even at the equator.[26] We point out that our predicted total photoreceptor-to-RPE ratio is not flat across the macula, and may have implications on theories of equalized metabolic load of RPE cells across the retina. This warrants further study using optimized photoreceptor imaging methods[62] to provide insight into this question by investigating the rod-to-RPE cell ratio in addition to the cone-to-RPE ratio, which may be more clinically relevant to disease. Interestingly, we found that reported ex vivo rod-to-RPE ratios were typically smaller than would be expected from our predicted curve.

IRAF Imaging

The resolution improvement from AOSLO applied to IRAF imaging allows for an alternative means of visualizing the RPE cell mosaic and microscopic structure of drusen in vivo, and with promising success across participants. IRAF offers several advantages over SWAF imaging, including near-perfect registration between the simultaneously captured RPE and photoreceptor mosaics, no image degradation from TCA blur, and no need for focus optimization to mitigate longitudinal chromatic aberration (LCA). The contribution of choroidal IRAF to RPE images is not obvious, but may be present as background and contribute to the lower RPE cell contrast than with SWAF. Liu et al.[16] have recently published images and analysis of the RPE mosaic in 12 normal human participants, using a similar system, reinforcing the validity of this method. However, both our results and theirs are limited by a lack of older participants. Further study is needed to demonstrate the utility in aging and diseased eyes, since melanin in the RPE decreases with age[35] and accumulates into complex granules.[32]

AO IRAF of subclinical drusen demonstrates potential for use in improved characterization of diseased eyes; this sensitivity could be particularly important for longitudinal studies examining the slow changes that occur to the RPE in AMD. The hyper-AF structures we observed within the region of drusen may arise from overlying RPE,[8] as melanin granules have been identified at the edges and irregularly distributed on top of drusen in ex vivo analyses of AMD tissue.[63] To our knowledge there are no reports of melanosomes in drusen, though other identified or unidentified components[64] may exhibit IRAF. Likewise, it remains unclear if the RPE mosaic remains intact or functional in these seemingly abnormal areas.

Comparison of IRAF and SWAF Morphology

The similar en face appearance of RPE cells in IRAF and SWAF was surprising because the latter is typically explained by displacement of lipofuscin granules by the nucleus in the basal cytoplasm, while melanin is thought to primarily occupy the apical cell cytoplasm and processes.[65] RPE cells also appear with a bright border and dark center in AOSLO studies where scattered light from the RPE is isolated from that of the photoreceptors, including cone-rod dystrophy,[14] AO-OCT,[18] and dark-field imaging.[15] The scattering properties of melanin[66] make it a candidate source of the reflectance signal in these studies, a contention bolstered by a recent OCT study showing melanin-dependent differences in the RPE band intensity and thickness in zebrafish.[67] The consistent appearance between AOSLO modalities may infer that melanin is more concentrated at cell borders in the cytoplasm, supported by one report of similar observations in tissue preparations.[68] Unfortunately, we were unable to find any published en face IRAF images of human RPE cells from histology for comparison as such data would be helpful to improve interpretation.

The subcellular morphologic observations in Figures 1 and 8 may be attributed to the relative concentration and distribution of fluorophores, known to differ between cells[69] and across the macula.[50,70] In SWAF, cells with continuous versus punctate hyper-AF borders may be the result of lipofuscin accumulation differences, particularly with age.[5,71,72] Differences in IRAF and SWAF subcellular structure at the same location reinforce that the modalities image separate fluorophores. Simultaneous IRAF and SWAF acquisition would provide a more ideal comparison, and when combined may enhance signal-to-noise and visibility of the RPE cell mosaic. While photoreceptors do not appear to waveguide AF emission from the RPE,[73] the observations of IRAF spots with similar size and location to overlying cones raise the possibility that the fluorescence pattern is influenced by waveguiding of the ingoing excitation radiation. This may have implications on the focus difference between best RPE image quality and peak SWAF MPV discussed earlier and in Supplementary Figure S12, though further investigation is necessary.

The observation of hyper-AF patches in AO SWAF against the more uniform appearance of IRAF is likely explained by tissue absorption differences. The difference of IRAF and SWAF excitation absorbed by hemoglobin[74] is considerable. We estimate that even a small 10-µm-diameter capillary absorbs ~20% of a 532-nm beam but just ~0.5% at 790 nm, where the difference increases drastically for larger vessels. The absorption difference by melanin is smaller, but a portion of the absorbed 790-nm radiation is converted to IRAF, while SWAF suffers a direct loss. The reduced impact of absorption on IRAF images may permit more accurate cell analysis.

Conclusions

In this study we showed that in vivo high-resolution imaging of the RPE mosaic can be effectively accomplished across the macula of normal participants, using both SWAF and IRAF imaging modalities, allowing for analysis and evaluation of cell morphology over this region. We provided here a normative in vivo dataset of RPE cells across the macula. These observations, along with those of the corresponding photoreceptor analysis, will be important to future investigations of morphology in the diseased eye. The comparison of high-resolution IRAF and SWAF images has allowed for identification of cellular and subcellular morphologic similarities and differences between modalities and hypotheses as to their origins. AO IRAF and AO SWAF images provide complementary information that may be instrumental for explaining changes in the photoreceptor-RPE complex in aging and disease.

Acknowledgments

The authors thank Rob Cooper for sharing the software used for photoreceptor marking in this study.

Supported by National Institutes of Health Grants EY001319, EY014375, EY004367, and EY007125, a grant to MMC from the Edward N. & Della L. Thome Memorial Foundation, and departmental startup funds to EAR. This research was also supported by unrestricted departmental grants from Research to Prevent Blindness. The funding organizations had no role in the design or conduct of this research.

Disclosure: **C.E. Granger**, Canon, Inc. (F); **Q. Yang**, Canon, Inc. (F), P; **H. Song**, None; **K. Saito**, Canon, Inc. (E, F), P; **K. Nozato**, Canon, Inc. (E, F), P; **L.R. Latchney**, None; **B.T. Leonard**, None; **M.M. Chung**, Canon, Inc. (F), Glaxo Smith Kline (C); **D.R. Williams**, Canon, Inc. (F, R), P; **E.A. Rossi**, Canon, Inc. (F), University of Rochester, (P)

References

1. Strauss O. The retinal pigment epithelium in visual function. *Physiol Rev.* 2005;85:845–881.

2. Sparrow JR, Hicks D, Hamel C. The retinal pigment epithelium in health and disease. *Curr Mol Med*. 2010;10:802–823.
3. Webb RH, Hughes GW, Delori FC. Confocal scanning laser ophthalmoscope. *Appl Opt*. 1987;26:1492–1499.
4. Wojtkowski M, Srinivasan VJ, Ko TH, Fujimoto JG, Kowalczyk A, Duker JS. Ultrahigh-resolution, high-speed, Fourier domain optical coherence tomography and methods for dispersion compensation. *Opt Express*. 2004;12:2404–2422.
5. Delori FC, Dorey CK, Staurenghi G, Arend O, Goger DG, Weiter JJ. In vivo fluorescence of the ocular fundus exhibits retinal pigment epithelium lipofuscin characteristics. *Invest Ophthalmol Vis Sci*. 1995;36:718–729.
6. von Rückmann A, Fitzke FW, Bird AC. Distribution of fundus autofluorescence with a scanning laser ophthalmoscope. *Br J Ophthalmol*. 1995;79:407–412.
7. Keilhauer CN, Delori FC. Near-infrared autofluorescence imaging of the fundus: visualization of ocular melanin. *Invest Ophthalmol Vis Sci*. 2006;47:3556–3564.
8. Spaide RF, Curcio CA. Drusen characterization with multimodal imaging. *Retina*. 2010;30:1441–1454.
9. Holz FG, Pauleikhoff D, Klein R, Bird AC. Pathogenesis of lesions in late age-related macular disease. *Am J Ophthalmol*. 2004;137:504–510.
10. Holz FG, Bindewald-Wittich A, Fleckenstein M, Dreyhaupt J, Scholl HPN, Schmitz-Valckenberg S. Progression of geographic atrophy and impact of fundus autofluorescence patterns in age-related macular degeneration. *Am J Ophthalmol*. 2007;143:463–472.e2.
11. Liang J, Williams DR, Miller DT. Supernormal vision and high-resolution retinal imaging through adaptive optics. *J Opt Soc Am A*. 1997;14:2884–2892.
12. Gray DC, Merigan W, Wolfing JI, et al. In vivo fluorescence imaging of primate retinal ganglion cells and retinal pigment epithelial cells. *Opt Express*. 2006;14:7144–7158.
13. Morgan JIW, Dubra A, Wolfe R, Merigan WH, Williams DR. In vivo autofluorescence imaging of the human and macaque retinal pigment epithelial cell mosaic. *Invest Ophthalmol Vis Sci*. 2009;50:1350–1359.
14. Roorda A, Zhang Y, Duncan JL. High-resolution in vivo imaging of the RPE mosaic in eyes with retinal disease. *Invest Ophthalmol Vis Sci*. 2007;48:2297–2303.
15. Scoles D, Sulai YN, Dubra A. In vivo dark-field imaging of the retinal pigment epithelium cell mosaic. *Biomed Opt Express*. 2013;4:1710–1723.
16. Liu T, Jung H, Liu J, Droettboom M, Tam J. Noninvasive near infrared autofluorescence imaging of retinal pigment epithelial cells in the human retina using adaptive optics. *Biomed Opt Express*. 2017;8:4348–4360.
17. Torti C, Považay B, Hofer B, et al. Adaptive optics optical coherence tomography at 120,000 depth scans/s for non-invasive cellular phenotyping of the living human retina. *Opt Express*. 2009;17:19382–19400.
18. Liu Z, Kocaoglu OP, Miller DT. 3D imaging of retinal pigment epithelial cells in the living human retina. *Invest Ophthalmol Vis Sci*. 2016;57:OCT533–OCT543.
19. Tam J, Liu J, Dubra A, Fariss R. In vivo imaging of the human retinal pigment epithelial mosaic using adaptive optics enhanced indocyanine green ophthalmoscopy. *Invest Ophthalmol Vis Sci*. 2016;57:4376–4384.
20. Engelbrecht NE, Freeman J, Sternberg P, et al. Retinal pigment epithelial changes after macular hole surgery with indocyanine green-assisted internal limiting membrane peeling. *Am J Ophthalmol*. 2002;133:89–94.
21. Narayanan R, Kenney MC, Kamjoo S, et al. Toxicity of indocyanine green (ICG) in combination with light on retinal pigment epithelial cells and neurosensory retinal cells. *Curr Eye Res*. 2005;30:471–478.
22. Rossi EA, Rangel-Fonseca P, Parkins K, et al. In vivo imaging of retinal pigment epithelium cells in age related macular degeneration. *Biomed Opt Express*. 2013;4:2527–2539.
23. Zhang J, Yang Q, Saito K, Nozato K, Williams DR, Rossi EA. An adaptive optics imaging system designed for clinical use. *Biomed Opt Express*. 2015;6:2120–2137.
24. Yang Q, Zhang J, Nozato K, et al. Closed-loop optical stabilization and digital image registration in adaptive optics scanning light ophthalmoscopy. *Biomed Opt Express*. 2014;5:3174–3191.
25. Dorey CK, Wu G, Ebenstein D, Garsd A, Weiter JJ. Cell loss in the aging retina. Relationship to lipofuscin accumulation and macular degeneration. *Invest Ophthalmol Vis Sci*. 1989;30:1691–1699.
26. Gao H, Hollyfield JG. Aging of the human retina: differential loss of neurons and retinal pigment epithelial cells. *Invest Ophthalmol Vis Sci*. 1992;33:1–17.
27. Panda-Jonas S, Jonas JB, Jakobczyk-Zmija M. Retinal pigment epithelial cell count, distribution, and correlations in normal human eyes. *Am J Ophthalmol*. 1996;121:181–189.
28. Gibbs D, Cideciyan AV, Jacobson SG, Williams DS. Retinal pigment epithelium defects in humans and mice with mutations in MYO7A: imaging melanosome-specific autofluorescence. *Invest Ophthalmol Vis Sci*. 2009;50:4386–4393.
29. Schmitz-Valckenberg S, Lara D, Nizari S, et al. Localisation and significance of in vivo near-infrared autofluorescent signal in retinal imaging. *Br J Ophthalmol*. 2011;95:1134–1139.
30. Sparrow JR, Nakanishi K, Parish CA. The lipofuscin fluorophore A2E mediates blue light–induced damage to retinal pigmented epithelial cells. *Invest Ophthalmol Vis Sci*. 2000;41:1981–1989.
31. Sparrow JR, Parish CA, Hashimoto M, Nakanishi K. A2E, a lipofuscin fluorophore, in human retinal pigmented epithelial cells in culture. *Invest Ophthalmol Vis Sci*. 1999;40:2988–2995.
32. Feeney L. Lipofuscin and melanin of human retinal pigment epithelium: fluorescence, enzyme cytochemical, and ultrastructural studies. *Invest Ophthalmol Vis Sci*. 1978;17:583–600.
33. Ueda K, Zhao J, Kim HJ, Sparrow JR. Photodegradation of retinal bisretinoids in mouse models and implications for macular degeneration. *Proc Natl Acad Sci U S A*. 2016;113:6904–6909.
34. Boulton M, Dayhaw-Barker P. The role of the retinal pigment epithelium: topographical variation and ageing changes. *Eye*. 2001;15:384–389.
35. Sarna T, Burke JM, Korytowski W, et al. Loss of melanin from human RPE with aging: possible role of melanin photooxidation. *Exp Eye Res*. 2003;76:89–98.
36. Kellner U, Kellner S, Weber BHF, Fiebig B, Weinitz S, Ruether K. Lipofuscin- and melanin-related fundus autofluorescence visualize different retinal pigment epithelial alterations in patients with retinitis pigmentosa. *Eye*. 2008;23:1349–1359.
37. Kellner U, Kellner S, Weinitz S. Fundus autofluorescence (488 nm) and near-infrared autofluorescence (787 nm) visualize different retinal pgiment epithelium alterations in patients with age-related macular degeneration. *Retina*. 2010;30:6–15.
38. Sparrow JR, Duncker T. Fundus autofluorescence and RPE lipofuscin in age-related macular degeneration. *J Clin Med*. 2014;3:1302–1321.
39. Dubra A, Sulai Y. Reflective afocal broadband adaptive optics scanning ophthalmoscope. *Biomed Opt Express*. 2011;2:1757–1768.

Investigative Ophthalmology & Visual Science

40. Yang Q, Yin L, Nozato K, et al. Calibration-free sinusoidal rectification and uniform retinal irradiance in scanning light ophthalmoscopy. *Opt Lett*. 2015;40:85–88.
41. Vinas M, Dorronsoro C, Cortes D, Pascual D, Marcos S. Longitudinal chromatic aberration of the human eye in the visible and near infrared from wavefront sensing, double-pass and psychophysics. *Biomed Opt Express*. 2015;6:948–962.
42. Huang Z, Zeng H, Hamzavi I, et al. Cutaneous melanin exhibiting fluorescence emission under near-infrared light excitation. *J Biomed Opt*. 2006;11:034010.
43. Harmening WM, Tiruveedhula P, Roorda A, Sincich LC. Measurement and correction of transverse chromatic offsets for multi-wavelength retinal microscopy in the living eye. *Biomed Opt Express*. 2012;3:2066–2077.
44. Rangel-Fonseca P, Gómez-Vieyra A, Malacara-Hernández D, Wilson MC, Williams DR, Rossi EA. Automated segmentation of retinal pigment epithelium cells in fluorescence adaptive optics images. *J Opt Soc Am A*. 2013;30:2595–2604.
45. Li KY, Roorda A. Automated identification of cone photoreceptors in adaptive optics retinal images. *J Opt Soc Am A*. 2007;24:1358–1363.
46. Laser Institute of America. *ANSI Z136.1 - 2014, American National Standard for Safe Use of Lasers*. Orlando, FL: Laser Institute of America; 2014.
47. Morgan JIW, Hunter JJ, Merigan WH, Williams DR. The reduction of retinal autofluorescence caused by light exposure. *Invest Ophthalmol Vis Sci*. 2009;50:6015–6022.
48. Curcio CA, Sloan KR, Kalina RE, Hendrickson AE. Human photoreceptor topography. *J Comp Neurol*. 1990;292:497–523.
49. Masella BD, Williams DR, Fischer WS, Rossi EA, Hunter JJ. Long-term reduction in infrared autofluorescence caused by infrared light below the maximum permissible exposure. *Invest Ophthalmol Vis Sci*. 2014;55:3929–3938.
50. Wing GL, Blanchard GC, Weiter JJ. The topography and age relationship of lipofuscin concentration in the retinal pigment epithelium. *Invest Ophthalmol Vis Sci*. 1978;17:601–607.
51. Weiter JJ, Delori FC, Wing GL, Fitch KA. Retinal pigment epithelial lipofuscin and melanin and choroidal melanin in human eyes. *Invest Ophthalmol Vis Sci*. 1986;27:145–152.
52. Snodderly DM, Brown PK, Delori FC, Auran JD. The macular pigment, I: absorbance spectra, localization, and discrimination from other yellow pigments in primate retinas. *Invest Ophthalmol Vis Sci*. 1984;25:660–673.
53. Bone RA, Landrum JT, Cains A. Optical density spectra of the macular pigment in vivo and in vitro. *Vision Res*. 1992;32:105–110.
54. Watzke RC, Soldevilla JD, Trune DR. Morphometric analysis of human retinal pigment epithelium: correlation with age and location. *Curr Eye Res*. 1993;12:133–142.
55. Harman AM, Fleming PA, Hoskins RV, Moore SR. Development and aging of cell topography in the human retinal pigment epithelium. *Invest Ophthalmol Vis Sci*. 1997;38:2016–2026.
56. Del Priore LV, Kuo Y-H, Tezel TH. Age-related changes in human RPE cell density and apoptosis proportion in situ. *Invest Ophthalmol Vis Sci*. 2002;43:3312–3318.
57. Ach T, Huisingh C, McGwin G Jr, et al. Quantitative autofluorescence and cell density maps of the human retinal pigment epithelium. *Invest Ophthalmol Vis Sci*. 2014;55:4832–4841.
58. Bhatia SK, Rashid A, Chrenek MA, et al. Analysis of RPE morphometry in human eyes. *Mol Vis*. 2016;22:898–916.
59. Song H, Chui TYP, Zhong Z, Elsner AE, Burns SA. Variation of cone photoreceptor packing density with retinal eccentricity and age. *Invest Ophthalmol Vis Sci*. 2011;52:7376–7384.
60. Ts'o MOM, Friedman E. The retinal pigment epithelium: III, growth and development. *Arch Ophthalmol*. 1968;80:214–216.
61. Ach T, Tolstik E, Messinger JD, Zarubina AV, Heintzmann R, Curcio CA. Lipofuscin redistribution and loss accompanied by cytoskeletal stress in retinal pigment epithelium of eyes with age-related macular degeneration. *Invest Ophthalmol Vis Sci*. 2015;56:3242–3252.
62. Dubra A, Sulai Y, Norris JL, et al. Noninvasive imaging of the human rod photoreceptor mosaic using a confocal adaptive optics scanning ophthalmoscope. *Biomed Opt Express*. 2011;2:1864–1876.
63. Tong Y, Ben Ami T, Hong S, et al. Hyperspectral autofluorescence imaging of drusen and retinal pigment epithelium in donor eyes with age-related macular degeneration. *Retina*. 2016;36:S127–S136.
64. Wang L, Clark ME, Crossman DK, et al. Abundant lipid and protein components of drusen. *PLoS One*. 2010;5:e10329.
65. Sarna T. New trends in photobiology: properties and function of the ocular melanin: a photobiophysical view. *J Photochem Photobiol B*. 1992;12:215–258.
66. Meredith P, Sarna T. The physical and chemical properties of eumelanin. *Pigment Cell Res*. 2006;19:572–594.
67. Wilk MA, Huckenpahler AL, Collery RF, Link BA, Carroll J. The effect of retinal melanin on optical coherence tomography images. *Trans Vis Sci Tech*. 2017;6(2):8.
68. Zinn KM, Marmor MF. *The Retinal Pigment Epithelium*. Cambridge, MA: Harvard University Press; 1979.
69. Burke JM, Hjelmeland LM. Mosaicism of the retinal pigment epithelium: seeing the small picture. *Mol Interv*. 2005;5:241–249.
70. Schmidt SY, Peisch RD. Melanin concentration in normal human retinal pigment epithelium: regional variation and age-related reduction. *Invest Ophthalmol Vis Sci*. 1986;27:1063–1067.
71. Feeney-Burns L, Hilderbrand ES, Eldridge S. Aging human RPE: morphometric analysis of macular, equatorial, and peripheral cells. *Invest Ophthalmol Vis Sci*. 1984;25:195–200.
72. Delori FC, Goger DG, Dorey CK. Age-related accumulation and spatial distribution of lipofuscin in RPE of normal subjects. *Invest Ophthalmol Vis Sci*. 2001;42:1855–1866.
73. Prieto PM, McLellan JS, Burns SA. Investigating the light absorption in a single pass through the photoreceptor layer by means of the lipofuscin fluorescence. *Vision Res*. 2005;45:1957–1965.
74. Jacques SL. Optical properties of biological tissues: a review. *Phys Med Biol*. 2013;58:R37–R61.

Investigative Ophthalmology & Visual Science